analytical chemistry

pubs.acs.org/ac

Article

Electrochemical Aptasensing of SARS-CoV-2 Based on Triangular Prism DNA Nanostructures and Dumbbell Hybridization Chain Reaction

Yu Jiang, Xifeng Chen, Ninghan Feng,* and Peng Miao*

Cite This: *Anal. Chem.* 2022, 94, 14755−14760

Read Online

ACCESS | Metrics & More | Article Recommendations | Supporting Information

ABSTRACT: Development of convenient, accurate, and sensitive methods for rapid screening of severe acute respiratory syndrome-coronavirus 2 (SARS-CoV-2) infection is highly desired. In this study, we have developed a facile electrochemical aptasensor for the detection of the SARS-CoV-2 S1 protein amplified by dumbbell hybridization chain reaction (DHCR). A triangular prism DNA (TPDNA) nanostructure is first assembled and modified at the electrode interface. Due to the multiple thiol anchors, the immobilization is quite stable. The TPDNA nanostructure also provides an excellent scaffold for better molecular recognition efficiency on the top single-strand region (DHP0). The aptamer sequence toward the SARS-CoV-2 S1 protein is previously localized by partial hybridization with DHP0. In the presence of the target protein, the aptamer sequence is displaced and DHP0 is exposed. After further introduction of the fuel stands of DHCR, compressed DNA linear assembly occurs, and the product can be stacked on the TPDNA nanostructure for the enrichment of electrochemical species. This electrochemical method successfully detects the target protein in clinical samples, which provides a simple, robust, and accurate platform with great potential utility.

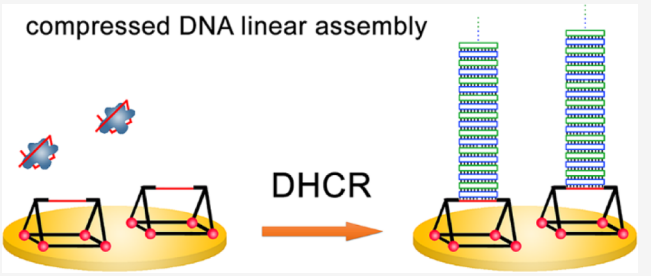

Coronaviruses (CoVs) are large enveloped nonsegmented RNA viruses decorated with club-shaped glycosylated spike (S) structural proteins, which cause respiratory tract disorders.[1−3] Severe acute respiratory syndrome-coronavirus 2 (SARS-CoV-2) was known since 2019, which belonged to the beta-CoV family. SARS-CoV-2-mediated infection was declared "COVID-19 pandemic" by the World Health Organization in March 2020. Although the fatality rate is low in humans, it is highly infectious compared with SARS-CoV and Middle East respiratory syndrome (MERS) coronavirus, which caused the outbreaks of SARS and MERS in 2003 and 2012, respectively.[4] In addition, the S protein of SARS-CoV-2 has been undergoing mutations, and the glycosylation degree is responsible for the viral infectivity variation.[5] Due to the severity of the COVID-19 pandemic and the continued multiple variations of SARS-CoV-2, highly sensitive and precise quantification methods are required, which should also be updated with time.[6,7] In the early stage of the COVID-19 outbreak, DNA sequencing was applied for accurate determination of infection.[8] Since it was quite expensive and required rigorous laboratory environments, quantitative reverse transcription-polymerase chain reaction was then introduced as the standard assay for the diagnosis, which offered sufficient sensitivity toward early diagnosis of the infection. However, several limitations still exist. The rate of false-negative result is relatively high. Quantifications of immunoglobulin M (IgM) or immunoglobulin G (IgG) antibodies in serum have also been developed to compensate for the deficiencies of nucleic acid detection. However, IgM and IgG detections were quite delayed since the onset of symptoms. Currently, various biosensors have been employed as tools for the diagnosis of COVID-19, which have the merits of fast response, high sensitivity, low cost, and so on. For example, Li's group fabricated covalent organic framework capsules with digestible zeolitic imidazolate framework-90 and proposed a visual colorimetric approach for SARS-CoV-2 RNA.[9] Wang et al. developed a CRISPR-Cas13 amplification principle for the profiling of SARS-CoV-2 and its mutated variants.[10]

For the specific diagnosis, SARS-CoV-2 itself and its structural proteins including the S protein, nucleocapsid (N), matrix (M), and small envelop (E) could be superior targets. Among them, the S protein is critical for the adhesion to host cells, which mediates the interaction of the angiotensin-converting enzyme-2 with the receptor-binding domain. Therefore, it is an important biomarker for serological analysis. Yang's group have selected and optimized several aptamers toward the receptor-binding domain of the S protein.[11] Several

Received: August 4, 2022
Accepted: October 5, 2022
Published: October 14, 2022

Scheme 1. Illustrations of the Assembly of TPDNA, Multiple Thiol-Aided Electrode Modification, Aptamer-Mediated Target Protein Recognition, and Subsequent DHCR Process on Top of TPDNA

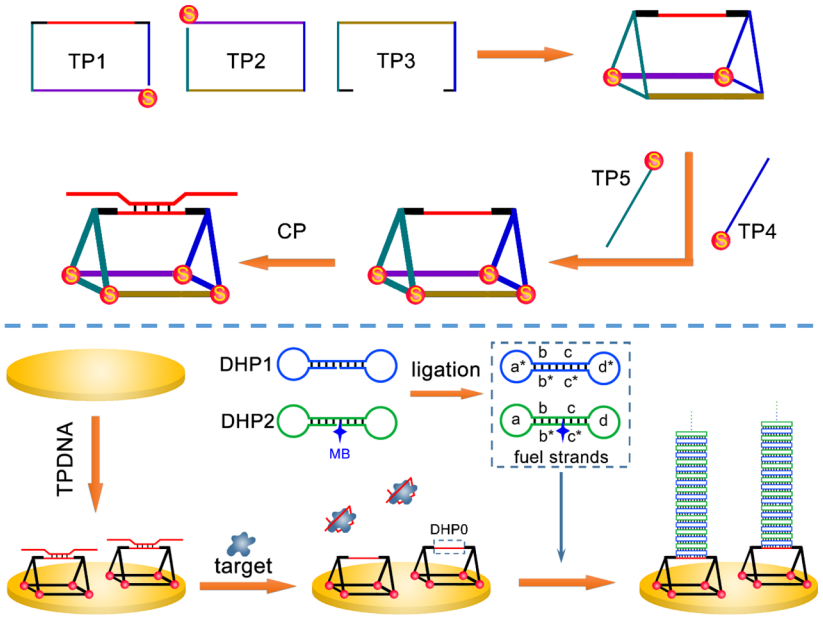

other groups have also made good use of the aptamers to target the S protein for highly sensitive and selective analysis.[12,13] Herein, we develop a novel electrochemical aptasensor for the SARS-CoV-2 S1 protein with optimized molecular recognition and signal amplification.

DNA nanostructures have been widely studied and applied since they offer many promising merits like high structural rigidity and biocompatibility.[14,15] For example, DNA triangular prism (TPDNA) is a three-dimensional DNA motif, which can be used as the template for the growth of new materials, vehicle for drug delivery, and excellent scaffold for the organization of additional DNA nanostructures.[16] Xu's group engineered TPDNA as a dual recognition nanoprobe toward the investigation of the relationship between K^+ and pH in lysosomes.[17] Li's group fabricated DNA logic nanodevices for in situ operation inside living cells based on TPDNA as the logic-controlling element.[18] In this study, the reactions occur on TPDNA nanostructures, which are previously modified at the electrode. Compressed DNA linear assembly can be achieved on top of TPDNA through dumbbell hybridization chain reaction (DHCR), which provides a significantly amplified electrochemical response. The limit of detection (LOD) for the analysis of target protein as low as 0.75 fM is obtained, and satisfactory practical utility is confirmed. The proposed method can be applied as a promising tool for direct detection of COVID-19.

RESULTS AND DISCUSSION

Biosensing Principle. A detailed working mechanism is illustrated in Scheme 1. Generally, TPDNA is first assembled from five single-stranded DNA as the three-dimensional scaffold for target recognition and signal amplification.[19] Four of them contain thiol groups at the end of each strand, and the rectangle bottom of the constructed TPDNA possesses multiple thiol anchors. As a result, the immobilization of the DNA scaffold at the gold electrode is much stable and firm compared with single thiol-based modification.[20,21] Surface-confined molecule recognition always shows poor performances compared with its counterparts in solution.[22] A disordered single-stranded DNA layer at the electrode surface might hinder effective capture of targets. Therefore, we take good advantage of the three-dimensional DNA scaffold for molecule recognition to control optimized spatial orientation, which minimizes the crowding effects and benefits effective recognition.[23] Herein, the single-stranded edge of TPDNA (DHP0) is applied as the trigger of DHCR, which involves the process of compressed DNA linear assembly and shows merits for electrochemical biosensing.[24] Initially, DHP0 is blocked by capture probe (CP), the aptamer of the S1 protein. Its secondary structure is shown in Figure S1a. The middle section of the CP is attached on TPDNA through hybridization. The reactions can be confirmed by performing polyacrylamide gel electrophoresis (PAGE). After mixing CP and TP1, a new band appears in the image. The mixture migrates slower than single-stranded DNA probes, demonstrating successful formation of a duplex. However, after further introduction of the target protein, CP is conjugated with target protein and the TP1 strand is displaced (Figure S1b). The released single-stranded region of TP1 (DHP0) can be applied as the trigger for further DHCR. DHP1 and DHP2 are the two fuel strands that constitute the compressed long linear DNA at the electrode surface, which are previously ligated before reaction. Since DHP2 is labeled with methylene blue (MB), by measuring the signal of MB from stacked DHCR product, the concentration of target protein can be evaluated. The ligation and TPDNA assembly events can be confirmed by employing exonuclease I, which cleaves single-stranded DNA (Figure S1c). With the ligase-catalyzed reaction, the digestion of circular DHP1 and DHP2 is resisted, and the bands are kept at the desired positions of the PAGE image. Similarly, the assembled TPDNA are mainly composed of double-stranded scaffolds, which cannot be digested by exonuclease I. A significant band with a large molecule weight is shown, which is ascribed to the three-dimensional DNA nanostructure. However, with the denaturation of these strands before

https://doi.org/10.1021/acs.analchem.2c03401
Anal. Chem. 2022, 94, 14755−14760

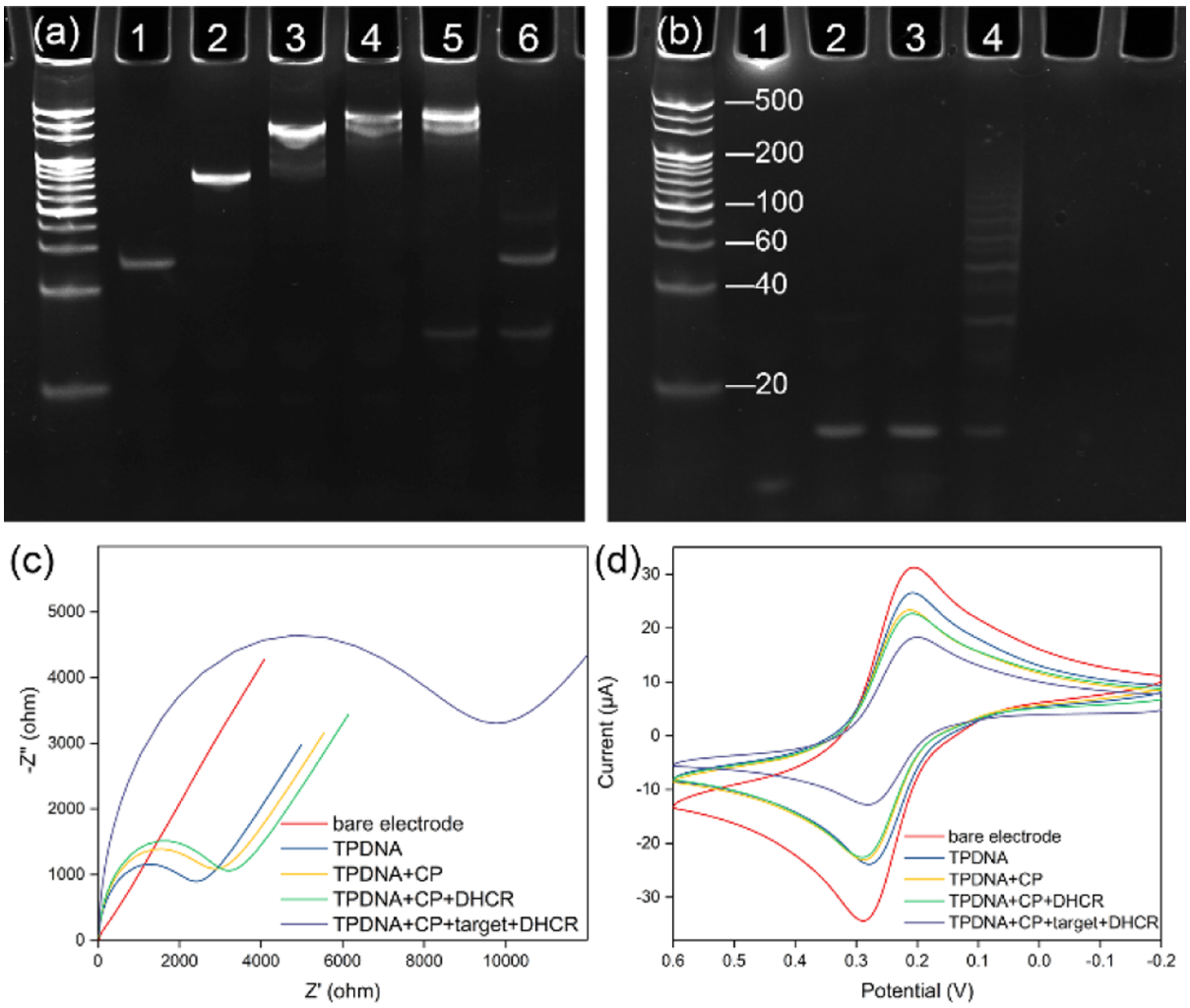

Figure 1. (a) Polyacrylamide gel electrophoresis analysis: (1) TP1; (2) TP1, TP2; (3) TP1, TP2, TP3; (4) TP1, TP2, TP3, TP4, TP5; (5) TP1, TP2, TP3, TP4, TP5, CP; (6) DHP0, CP. (b) Polyacrylamide gel electrophoresis analysis: (1) DHP0; (2) DHP1; (3) DHP1, DHP2; (4) DHP0, DHP1, DHP2. (c) Nyquist diagrams and (d) cyclic voltammograms of a bare electrode, a TPDNA-modified electrode, after incubation with CP and DHCR procedure in the absence and presence of the target protein.

assembly, they can be quickly digested, and no bands are observed in the PAGE image.

TPDNA and DHCR Characterizations. To characterize the step-by-step assembly processes of TPDNA and DHCR, PAGE experiments are performed to probe the molecule weights of the reaction products. As shown in Figure 1a, one, two, three, and five strands of TPDNA are mixed. With the increase of the number of introduced strands, more strands participate in the DNA nanostructure construction, and the generated complex shows larger molecule weights. After further addition of CP, the intensity of the band becomes brighter, demonstrating successful conjugation of CP and TPDNA. In addition, DHP0 as the trigger of DHCR is synthesized independently, which is mixed with CP directly. The resulted product shows a larger molecule weight, and the appeared band runs much slower. DHCR can also be confirmed by PAGE analysis. As shown in Figure 1b, in the absence of DHP0, the mixture of DHP1 and DHP2 cannot form larger DNA nanostructures. However, after induced by the DHP0-mediated dumbbell opening phenomenon, smear bands can be observed in the gel, which are regarded as the products of DHCR.

Electrochemical Characterization of Sensing Feasibility. To verify the feasibility of the electrochemical sensing strategy, electrochemical impedance spectroscopy (EIS) and cyclic voltammetry (CV) are carried out to identify the stepwise properties of modified electrodes.[25] As depicted in the nyquist plots, a bare gold electrode shows excellent electrical conductivity reflected by the straight line; after being modified with TPDNA, a semicircle domain is generated, which is due to the repellent reaction between immobilized DNA and $[Fe(CN)_6]^{3-/4-}$;[26] after further incubation with CP, a slight larger semicircle demonstrates increased charge-transfer resistance by the attached CP; in the presence of the target, CP is released and DHCR can be carried out with stacked fuel strands at the electrode interface, leading to significantly an increased semicircle domain. On the other hand, in the absence of the target, the diameter of the semicircle is nearly the same as that of the TPDNA modified electrode, verifying that DHCR cannot be carried out without a target protein. CV curves recorded after these reaction steps and the variations of current peaks are consistent with EIS results, demonstrating the feasibility of the sensing strategy.

Electrochemical Quantification of the Target Protein. To achieve the best analytical performances of the sensing

https://doi.org/10.1021/acs.analchem.2c03401
Anal. Chem. 2022, 94, 14755−14760

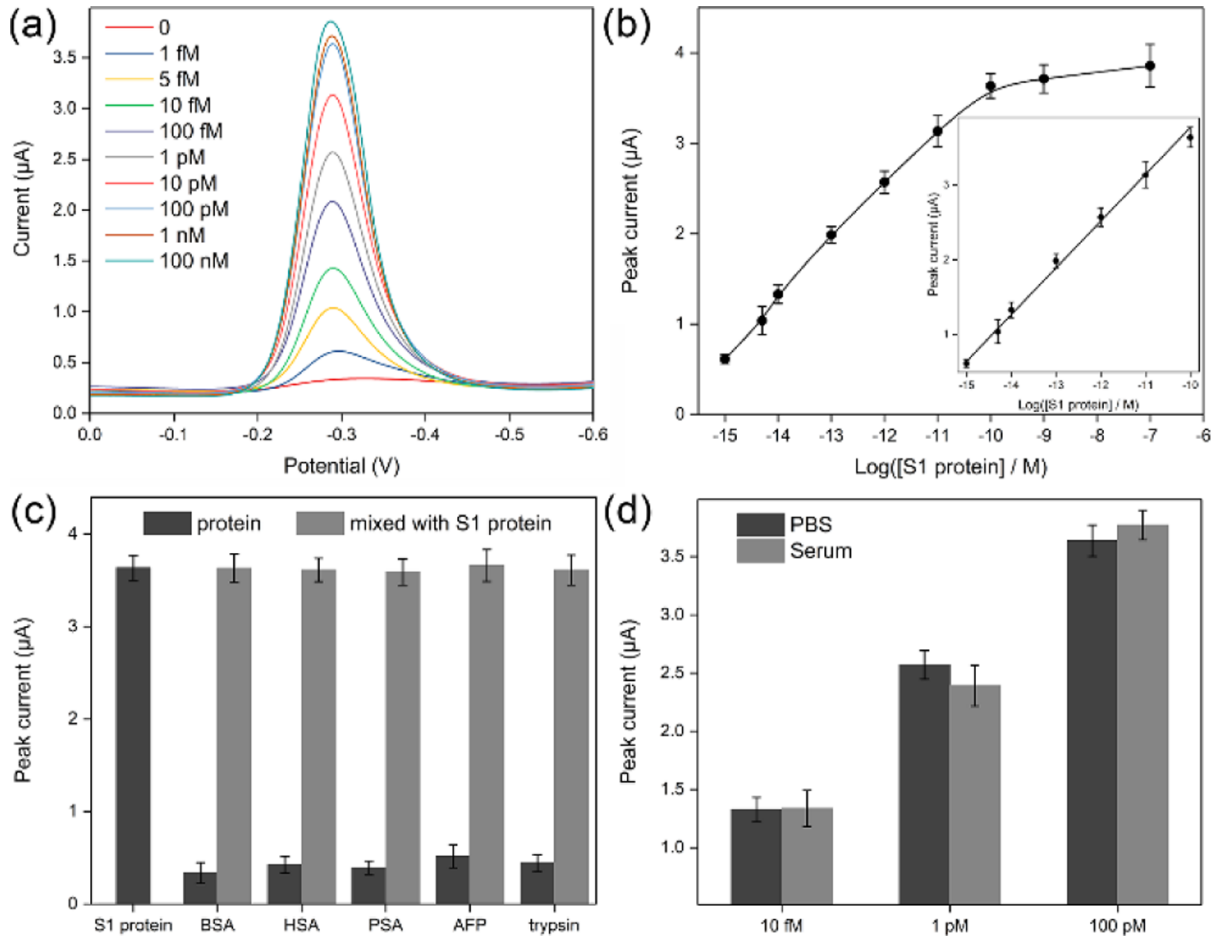

Figure 2. (a) Square wave voltammograms for the detection of the target with the concentrations of 0, 1 fM, 5 fM, 10 fM, 100 fM, 1 pM, 10 pM, 100 pM, 1 nM, and 100 nM. (b) Calibration curve reflecting the relationship between peak current and the logarithm of target concentration. Inset is the linear range. (c) Selectivity investigation by electrochemical measurements of the S1 protein, BSA, HSA, PSA, AFP, and trypsin. (d) Histograms for electrochemical detection of different concentrations of the target spiked in PBS and serum samples.

strategy, several key parameters should be optimized by comparing the charge-transfer resistance of EIS and the current peak of square wave voltammetry (SWV). 0.9 μM TPDNA for electrode immobilization, 45 min for target incubation, and 90 min for DHCR are selected for the following experiments (Figure S2). Under these optimal conditions, we have further explored the SWV curves for the analysis of the target protein. As shown in Figure 2a, with the increase of the target protein, more CP strands can be displaced from the TPDNA at the electrode interface. More fuel strands with MB are thus stacked during the DHCR process, leading to increased SWV peak intensities. The detailed relationship between peak intensity and the logarithm of target protein concentration is shown in Figure 2b. A good linear relationship is established from 1 fM to 100 pM with the regression equation as follows

$$y = 10.019 + 0.625 \times (n = 3, R^2 = 0.996)$$

in which y stands for the peak current and x is the logarithmic protein concentration. The LOD of this sensor is calculated to be 0.75 fM (signal-to-noise ratio = 3).[35] The analytical performances show superiority compared with recently developed assays (Table 1). Meanwhile, the detection time is acceptable. We have then employed bovine serum albumin, human serum albumin, prostate-specific antigen, alpha-fetoprotein, and trypsin as potential interfering molecules. As shown in Figure 2c, without mixing with the S1 protein, they could not induce a significant electrochemical response. After the blending procedure, the obtained peak currents are similar with those of pure S1 protein, demonstrating the excellent

Table 1. Comparison of the Analytical Performances of Recent SARS-CoV-2 Aptasensors[a]

technique	strategy	LOD (ng mL^{-1})	refs
colorimetry	aptamer-functionalized gold nanoparticles	812.3	27
colorimetry	G-quadruplex aptamer-based assay	101.5	28
PE	2D MOF-based aptasensor	72	29
fluorescence	protein-induced fluorescence enhancement	50	30
SWV	aptamer-modified electrode	5.07×10^{-1}	31
EIS	photo-induced force microscopic imaging of complex	6.6×10^{-2}	32
SPR	niobium carbide MXene quantum dots	4.9×10^{-3}	33
NSET	DNA-modified gold nanostar	1.3×10^{-4}	34
SWV	compressed DNA linear assembly on a TPDNA-modified electrode	3.8×10^{-5}	this work

[a]NSET, nanoparticle surface energy transfer spectroscopy; PE, photoelectrochemistry; SPR, surface plasmon resonance.

https://doi.org/10.1021/acs.analchem.2c03401
Anal. Chem. 2022, 94, 14755−14760

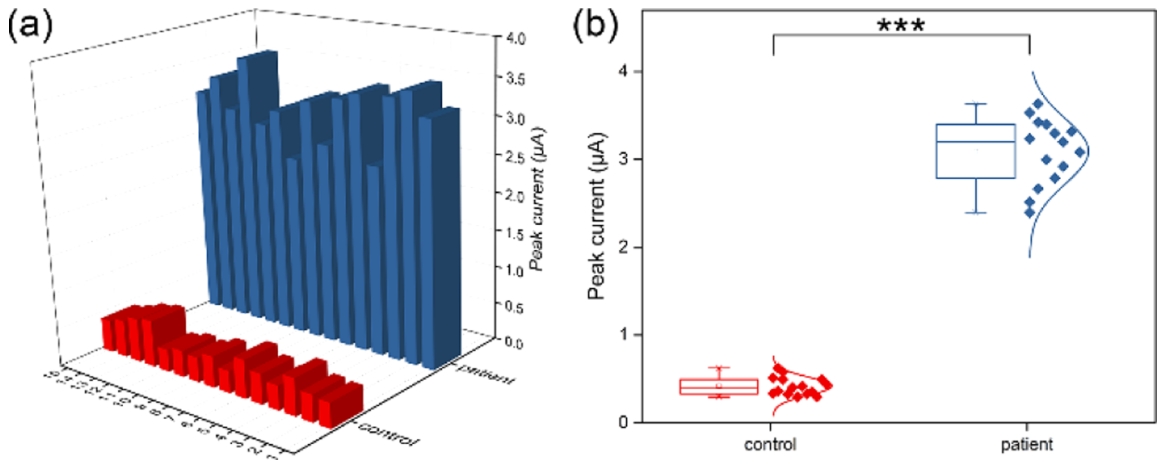

Figure 3. (a) Comparison of SWV responses toward the samples from patients and normal controls. (b) Box plot of SWV responses. The statistical significances are calculated by a *t*-test (***$p < 0.001$).

selectivity of this method. To further study the anti-interfering capability of the sensing system, different amounts of the S1 protein are spiked with serum, which are then applied for electrochemical reactions and measurements. The results are shown in Figure 2d. Since the sensing interface of the electrode is covered by the TPDNA which blocks the adsorption of potential interferences in the serum at the electrode, the electrochemical response mainly reflects the existence of the target protein. The electrochemical responses are in good accordance with those of the same concentration in phosphate-buffered solution conditions.

Application of the Electrochemical Detection in Clinical Samples. To assess the stability and reproducibility of this approach, we have first modified the gold electrodes with TPDNA and stored them for different times. Then, the electrodes are used for the detection of the target protein. The obtained SWV peak currents are compared. It is clear that after being stored for 2 weeks, the measured signal is still comparable with those of freshly treated electrodes, demonstrating good stability of the TPDNA sensing layer (Figure S3a). Reproducibility is also very important for accurate determination of trace biomarkers. Interassays with four independent DNA-modified electrodes are performed for the analysis of different levels of the target protein. The average relative standard deviations are less than 5%, verifying acceptable reproducibility (Figure S3b). We have then collected pharyngeal swab samples of healthy individuals and SARS-CoV-2 patients and performed more experiments to verify the utility of this method in biological samples. After being applied in the electrochemical method, the peak currents of the measured SWV curves are assessed and compared, shown in Figure 3a. Positive SARS-CoV-2 samples indeed produce significantly larger currents, which can be successfully distinguished from the control group (Figure 3b). Therefore, it is demonstrated to be a good complement of the current nucleic acid assay for COVID-19 diagnosis. To meet the requirements of high-throughput screening, the adaptation of this electrochemical sensing strategy into a portable analyzer with a screen-printed electrode array may be a beneficial attempt. In addition, by redesigning the sequences, the DHCR amplification strategy is also applicable for the detection of other targets.[36]

CONCLUSIONS

To reply to the rapid spread of SARS-CoV-2, we have performed a proof-of-concept demonstration of an ultrasensitive electrochemical strategy for the detection of spike protein. An aptamer is applied as the recognition element, which is first embedded in a TPDNA, blocking the initiation sequence of DHCR. The nanostructures provide suitable spatial environment for the interaction between the target and the aptamer. After specific recognition, the exposed single-stranded region on top of the triangular prism is able to recruit a larger number of fuel strands for compressed DNA linear assembly, which shows merits of larger signal intensity compared with traditional HCR. The finally achieved analytical performances are excellent. The LOD is as low as 0.75 fM, which presents superiority than most commercial kits. To apply this electrochemical aptasensor to actual clinical practice, the reactions can be carried out on a screen-printed gold electrode for read-out coupled with a portable electrochemical analyzer.

ASSOCIATED CONTENT

Supporting Information

The Supporting Information is available free of charge at https://pubs.acs.org/doi/10.1021/acs.analchem.2c03401.

Experimental section; secondary structure of CP; PAGE demonstrations of the interaction between CP and the target protein, ligation of DHCR fuel strands, and assembly of TPDNA; optimization experiments for reaction conditions; and DNA sequences (PDF)

AUTHOR INFORMATION

Corresponding Authors

Ninghan Feng − *The Affiliated Wuxi No. 2 People's Hospital of Nanjing Medical University, Wuxi 214000, China*; Email: n.feng@njmu.edu.cn

Peng Miao − *Suzhou Institute of Biomedical Engineering and Technology, Chinese Academy of Sciences, Suzhou 215163, China*; orcid.org/0000-0003-3993-4778; Email: miaopeng@sibet.ac.cn

Authors

Yu Jiang − *The Affiliated Wuxi No. 2 People's Hospital of Nanjing Medical University, Wuxi 214000, China*

https://doi.org/10.1021/acs.analchem.2c03401
Anal. Chem. 2022, 94, 14755−14760

Xifeng Chen − *Suzhou Institute of Biomedical Engineering and Technology, Chinese Academy of Sciences, Suzhou 215163, China*

Complete contact information is available at: https://pubs.acs.org/10.1021/acs.analchem.2c03401

Author Contributions

All authors have given approval to the final version of the manuscript.

Notes

The authors declare no competing financial interest.

■ ACKNOWLEDGMENTS

This work was supported by the Social Development Project of Jiangsu Province (BE2018629), China Postdoctoral Science Foundation (2019T120461), Postdoctoral Science Foundation of Jiangsu Province (CRO201904), and the Top-notch Talents Program of Wuxi (BJ2020035).

■ REFERENCES

(1) Ke, Z. L.; Oton, J.; Qu, K.; Cortese, M.; Zila, V.; McKeane, L.; Nakane, T.; Zivanov, J.; Neufeldt, C. J.; Cerikan, B.; Lu, J. M.; Peukes, J.; Xiong, X. L.; Kräusslich, H.-G.; Scheres, S. H. W.; Bartenschlager, R.; Briggs, J. A. G. *Nature* **2020**, *588*, 498−502.
(2) Perlman, S.; Netland, J. *Nat. Rev. Microbiol.* **2009**, *7*, 439−450.
(3) Menachery, V. D.; Yount, B. L.; Debbink, K.; Agnihothram, S.; Gralinski, L. E.; Plante, J. A.; Graham, R. L.; Scobey, T.; Ge, X. Y.; Donaldson, E. F.; Randell, S. H.; Lanzavecchia, A.; Marasco, W. A.; Shi, Z. L. L.; Baric, R. S. *Nat. Med.* **2015**, *21*, 1508−1513.
(4) de Wit, E.; van Doremalen, N.; Falzarano, D.; Munster, V. J. *Nat. Rev. Microbiol.* **2016**, *14*, 523−534.
(5) Li, Q. Q.; Wu, J. J.; Nie, J. H.; Zhang, L.; Hao, H.; Liu, S.; Zhao, C. Y.; Zhang, Q.; Liu, H.; Nie, L. L.; Qin, H. Y.; Wang, M.; Lu, Q.; Li, X. Y.; Sun, Q. Y.; Liu, J. K.; Zhang, L. Q.; Li, X. G.; Huang, W. J.; Wang, Y. C. *Cell* **2020**, *182*, 1284−1294.
(6) Lu, S. H.; Tong, X. H.; Han, Y.; Zhang, K.; Zhang, Y. Z.; Chen, Q. B.; Duan, J. Y.; Lei, X. L.; Huang, M. H.; Qiu, Y.; Zhang, D. Y.; Zhou, X.; Zhang, Y.; Yin, H. *Nat. Biomed. Eng.* **2022**, *6*, 286−297.
(7) Miao, P.; Chai, H.; Tang, Y. G. *ACS Nano* **2022**, *16*, 4726−4733.
(8) Wu, F.; Zhao, S.; Yu, B.; Chen, Y. M.; Wang, W.; Song, Z. G.; Hu, Y.; Tao, Z. W.; Tian, J. H.; Pei, Y. Y.; Yuan, M. L.; Zhang, Y. L.; Dai, F. H.; Liu, Y.; Wang, Q. M.; Zheng, J. J.; Xu, L.; Holmes, E. C.; Zhang, Y. Z. *Nature* **2020**, *579*, 265−269.
(9) Wang, M. H.; Lin, Y. X.; Lu, J. Y.; Sun, Z. W.; Deng, Y.; Wang, L.; Yi, Y. X.; Li, J. L.; Yang, J.; Li, G. X. *Chem. Eng. J.* **2022**, *429*, 132332.
(10) Wang, Y. X.; Zhang, Y.; Chen, J. B.; Wang, M. J.; Zhang, T.; Luo, W. X.; Li, Y. L.; Wu, Y. P.; Zeng, B.; Zhang, K. X.; Deng, R. J.; Li, W. M. *Anal. Chem.* **2021**, *93*, 3393−3402.
(11) Song, Y. L.; Song, J.; Wei, X. Y.; Huang, M. J.; Sun, M.; Zhu, L.; Lin, B. Q.; Shen, H. C.; Zhu, Z.; Yang, C. Y. *Anal. Chem.* **2020**, *92*, 9895−9900.
(12) Huang, G. Y.; Zhao, H. X.; Li, P.; Liu, J. J.; Chen, S. Y.; Ge, M. H.; Qin, M.; Zhou, G. L.; Wang, Y. T.; Li, S. F.; Cheng, Y. Z.; Huang, Q.; Wang, J. F.; Wang, H. Z.; Yang, L. B. *Anal. Chem.* **2021**, *93*, 16086−16095.
(13) Lewis, T.; Giroux, E.; Jovic, M.; Martic-Milne, S. *Analyst* **2021**, *146*, 7207−7217.
(14) Pei, H.; Zuo, X. L.; Zhu, D.; Huang, Q.; Fan, C. H. *Acc. Chem. Res.* **2014**, *47*, 550−559.
(15) Liu, X.; Meng, F.; Sun, R.; Wang, K.; Yu, Z.; Miao, P. *Chem. Commun.* **2021**, *57*, 2629−2632.
(16) Yang, Q. X.; Guo, Z. Z.; Liu, H.; Peng, R. Z.; Xu, L. J.; Bi, C.; He, Y. Q.; Liu, Q. L.; Tan, W. H. *J. Am. Chem. Soc.* **2021**, *143*, 232−240.
(17) Li, X. Q.; Liu, X. N.; Jia, Y. L.; Luo, X. L.; Chen, H. Y.; Xu, J. J. *Anal. Chem.* **2021**, *93*, 14892−14899.
(18) Du, Y.; Peng, P.; Li, T. *ACS Nano* **2019**, *13*, 5778−5784.
(19) Chai, H.; Miao, P. *Chin. Chem. Lett.* **2021**, *32*, 783−786.
(20) Chai, H.; Tang, Y. G.; Guo, Z. Z.; Miao, P. *Anal. Chem.* **2022**, *94*, 2779−2784.
(21) Abi, A.; Lin, M. H.; Pei, H.; Fan, C. H.; Ferapontova, E. E.; Zuo, X. L. *ACS Appl. Mater. Interfaces* **2014**, *6*, 8928−8931.
(22) Browne, W. R.; Feringa, B. L. *Nat. Nanotechnol.* **2006**, *1*, 25−35.
(23) Zhu, D.; Pei, H.; Yao, G. B.; Wang, L. H.; Su, S.; Chao, J.; Wang, L. H.; Aldalbahi, A.; Song, S. P.; Shi, J. Y.; Hu, J.; Fan, C. H.; Zuo, X. L. *Adv. Mater.* **2016**, *28*, 6860−6865.
(24) Miao, P.; Tang, Y. G. *Anal. Chem.* **2020**, *92*, 12026−12032.
(25) Han, Z. Y.; Li, H. K.; Zhu, Q. Q.; Yuan, R. R.; He, H. M. *Chin. Chem. Lett.* **2021**, *32*, 2865−2868.
(26) Shi, H.; Gong, Y. J.; Liang, Q. Z.; Li, J. L.; Xiang, Y.; Li, G. X. *Anal. Chem.* **2021**, *93*, 13382−13388.
(27) Aithal, S.; Mishriki, S.; Gupta, R.; Sahu, R. P.; Botos, G.; Tanvir, S.; Hanson, R. W.; Puri, I. K. *Talanta* **2022**, *236*, 122841.
(28) Gupta, A.; Anand, A.; Jain, N.; Goswami, S.; Anantharaj, A.; Patil, S.; Singh, R.; Kumar, A.; Shrivastava, T.; Bhatnagar, S.; Medigeshi, G. R.; Sharma, T. K. *Mol. Ther. Nucleic Acids* **2021**, *26*, 321−332.
(29) Jiang, Z. W.; Zhao, T. T.; Li, C. M.; Li, Y. F.; Huang, C. Z. *ACS Appl. Mater. Interfaces* **2021**, *13*, 49754−49761.
(30) Lee, J. M.; Kim, C. R.; Kim, S.; Min, J. H.; Lee, M.-H.; Lee, S. *Chem. Commun.* **2021**, *57*, 10222−10225.
(31) Idili, A.; Parolo, C.; Alvarez-Diduk, R.; Merkoçi, A. *ACS Sens.* **2021**, *6*, 3093−3101.
(32) Abrego-Martinez, J. C.; Jafari, M.; Chergui, S.; Pavel, C.; Che, D.; Siaj, M. *Biosens. Bioelectron.* **2022**, *195*, 113595.
(33) Chen, R. Y.; Kan, L.; Duan, F. H.; He, L. H.; Wang, M. H.; Cui, J.; Zhang, Z. H.; Zhang, Z. H. *Microchim. Acta* **2021**, *188*, 316.
(34) Pramanik, A.; Gao, Y.; Patibandla, S.; Mitra, D.; McCandless, M. G.; Fassero, L. A.; Gates, K.; Tandon, R.; Ray, P. C. *J. Phys. Chem. Lett.* **2021**, *12*, 2166−2171.
(35) Gegenschatz, S. A.; Chiappini, F. A.; Teglia, C. M.; Muñoz de la Peña, A.; Goicoechea, H. C. *Anal. Chim. Acta* **2022**, *1209*, 339342.
(36) Jiang, Y.; Chen, X. F.; Feng, N. H.; Miao, P. *Sens. Actuators, B* **2021**, *340*, 129952.